COMPUTATION OF PROP-FAN ENGINE INSTALLATION AERODYNAMICS

ICAS-84-5.5.3

C.W. Boppe and B.S. Rosen
Grumman Aerospace Corporation
Bethpage, New York

Abstract

A computational method has been enhanced to permit numerical evaluations of transonic aerodynamic phenomena associated with prop-fan engine installations. Comparisons with experimental data and results using other algorithms provide a basis for augmenting intuition to determine which aspects of the physical flow and the computerized flow simulation are most important. Features of the prop-fan slipstream and the engine nacelle are modeled. In addition, a wind tunnel test was conducted to study the interference effect generated by a simple nacelle which is embedded in a wing surface. Observations that relate to future engineering applications are included.

Nomenclature

Symbols

M	Mach Number
C_p	Pressure Coefficient
α	Angle-of-Attack
η	Wing Span Position
c	Chord Length
c_l	Section Lift Coefficient
C_L	Lift Coefficient
C_D	Drag Coefficient
C_M	Moment Coefficient
φ	Perturbation Velocity Potential
γ	Specific Heat Ratio
P	Pressure
q	Dynamic Pressure
r	Radial Distance
R	Slipstream Radius
F	Nacelle Shape Function
ξ, η	Skewed Coordinate System
Δ	Mesh Spacing, Increment
$\mathcal{C}$	Centerline
W	Slipstream Swirl Angle

Subscripts

MAC	Mean Aerodynamic Chord
∞	Free-Stream
x,y,z	Partial Derivatives
T	Total
i,j	Grid Indices

I. Introduction

High-speed ($M = 0.7, 0.8$) propellers called prop-fans provide a means for attaining propulsive efficiency levels that are higher than those for current technology turbofans. To ensure that the integrated prop-fan concept will truly advance total aircraft efficiency, the propulsor-airframe interference effect must be minimized. Many engine installation schemes have been proposed; these

include pusher, tractor, and counter-rotating designs. The tractor scheme is appropriate for initial computational investigations as it incorporates all of the geometric and aerodynamic aspects of the expected integration problem and, in a sense, represents the most difficult case for design. Since historical design efforts do not exist and the experimental data base is somewhat limited, the potential contribution that can be made by today's computational methods is high.

To date, one of the most extensive computational treatments of the prop-fan integration problem has been accomplished using "panel" methods[1]. This type of potential flow approach provided flexibility to treat the complex geometric arrangements anticipated and an attempt was made to predict the drag increments required to assess performance characteristics. One aspect of this approach that deserves further study is the ability to predict detailed chordwise pressure distributions which, at prop-fan transonic cruise conditions, will exhibit shock wave discontinuities. This would enhance the ability to predict wave drag losses and flow separation. A number of nonlinear, compressible flow, relaxation schemes[2-6] have been developed to treat this problem. Formulations for the classical transonic small perturbation equation, the full potential equation, and Euler's equations have been described. These studies provide good qualitative agreement with available experimental data but details of the pressure fields are not resolved. In some cases, flow separation impairs the comparisons. The lack of pressure field detail may, in part, explain the traditional failure of computational methods to predict absolute and most incremental drag effects which are needed during the design process for performance estimates. The designer is obliged to use the predicted shock wave strengths, locations, and wing spanwise loading to piece together the wave, lift-induced, and friction drag components.
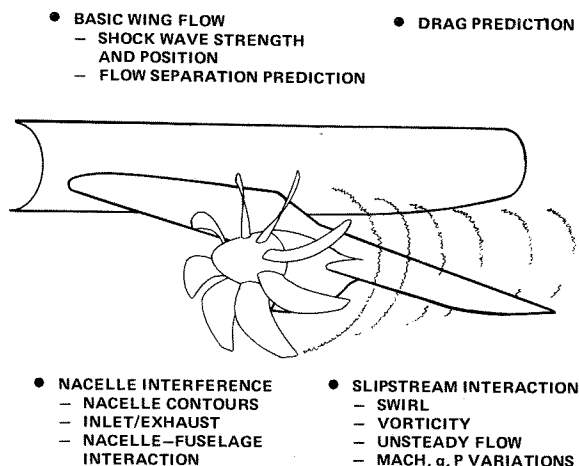
A numerical/experimental study was conducted to assess the ability of a relative high grid density computational method[7] to predict pressure details and incremental drag levels. This scheme features an extended transonic small-perturbation equation coupled with mesh-system embedding and simple planar boundary conditions which provide modeling flexibility comparable to that of panel methods. But perhaps most important, a high-density grid (100 points chordwise) is implemented to resolve flow details.

II. Problem Description

Prop-fan engine installations present a design problem to the configuration aerodynamicist that is quite different than that of turbofan engine installations.

Fundamentally, it can be expected that propulsion/airframe interaction phenomena will be considerably stronger for prop-fan arrangements primarily due to the anticipated proximity of airframe, propulsor components, and high-energy stream regions.

The most common installation now proposed features an engine nacelle which is embedded in the wing surface. The embedded nacelle, at high speeds, is expected to alter the wing shock wave pattern and spanload, and it might also induce the flow to separate. This arrangement has been sketched in Fig. 1. It should also be noted that, for some installations, the nacelle and fuselage might be sufficiently close to interact aerodynamically, further complicating the physical flow along with the engine inlet and exhaust flows.

● BASIC WING FLOW
 — SHOCK WAVE STRENGTH
   AND POSITION
 — FLOW SEPARATION PREDICTION

● DRAG PREDICTION

● NACELLE INTERFERENCE
 — NACELLE CONTOURS
 — INLET/EXHAUST
 — NACELLE—FUSELAGE
   INTERACTION

● SLIPSTREAM INTERACTION
 — SWIRL
 — VORTICITY
 — UNSTEADY FLOW
 — MACH, q, P VARIATIONS

R84-0628-001D

Fig. 1 Flow Simulation Considerations for Prop-Fan Engine Installation Applications

Prop-fan tractor concepts will be further compromised by the blade slipstream which will flow about the nacelle-wing combination. The rotating slipstream induces an upwash/downwash field in addition to variations in axial velocity, temperature, and total pressure. Embedded in this region will be discrete helical wakes emanating from the individual prop-fan blade surfaces. The resulting unsteady flow is expected to expand and redistribute various properties as it flows around, and is influenced by, the configuration surface components. Viscous effects will dissipate the slipstream flow as it proceeds downstream. It can be expected that the wave, lift-induced, and viscous drag components will increase unless these adverse interference effects are compensated for in the design process.

The designer who seeks a computational tool to augment the installation integration effort must decide which components of the problem should be modeled or represented to provide useful flow simulations. This is important because modeling the complete physical flow with all its attributes is not possible with current computational technology levels. Approximations must be made. A ranking of the importance of different problem components for a typical tractor application is provided below:
1. Basic Wing Flow Simulation
2. Nacelle Contour Interference
3. Slipstream Swirl
4. Slipstream q and P_T Increments
5. Engine Inlet and Exhaust Flows
6. Viscous Dissipation and Redistribution of Slipstream Flow.

This ranking is based on past experimental and computational studies[2-6]. Key elements must be treated and validated to (1) computationally predict drag increments or (2) provide sufficient flow details (shock position/strength, spanload, and separation prediction) to permit drag estimates to be composed external to the computational method. The scheme to be presented will address the first four items.

III. Basic Algorithm Description

The computational studies are performed using an extended transonic small-perturbation code[7]. Boundary conditions are imposed in the plane of the wing and the wake is represented by a double-valued plane of points across which a jump in the velocity potential is enforced. The flow equation contains extra cross-flow terms (when compared to the classical transonic small-perturbation equation) which make it possible to resolve shock waves with appreciable sweep:

$$[1 - M_\infty^2 - (\gamma + 1) M_\infty^2 \, \varphi_x - \frac{\gamma + 1}{2} M_\infty^2 \, \varphi_x^2] \, \varphi_{xx} - 2M_\infty^2 \, \varphi_y \, \varphi_{xy}$$
$$+ [1 - (\gamma - 1) M_\infty^2 \, \varphi_x] \, \varphi_{yy} + \varphi_{zz} = 0 \qquad (1)$$

Pressure coefficients on wing surfaces are computed using the following equation:

$$C_p = - [2\varphi_x + (1 - M_\infty^2) \, \varphi_x^2 + \varphi_y^2] \qquad (2)$$

In terms of flow equation and boundary condition complexity, the present formulation is somewhat more complicated than the small-perturbation formulation[2] but simpler than the full potential and Euler formulations[3-6]. A high-density grid system embedded along the wing span provides 100 evenly spaced grid points between the wing chord leading and trailing edges. Spanwise grid lines "cut" the wing at intervals which average between 5% and 7% of the wing half-span.

Wing viscous effects are approximated in the present method by coupling a modified Bradshaw boundary layer scheme[10] to the potential flow method. The modified chord technique of Nash & Tseng[11] is employed so that a two-dimensional boundary layer method can be extended to compute three-dimensional streamwise flows. Thus, the boundary layer is computed at streamwise strips along the wing span with no true spanwise viscous link. The mid-chord sweep angle is used as an "effective" sweep for this process. The computed boundary layer displacement thickness is added to the wing surface to provide an equivalent inviscid wing shape for analysis using the potential flow scheme. Noncon-

servative differencing is used and no attempt has been made to treat the true shock/boundary layer interaction.

IV. Clean Wing Flow Simulations

A number of investigators[2,3,5] have suggested that small-perturbation formulations are inadequate for treating the blunt, thick, supercritical airfoil sections that might be used for high-speed prop-fan configuration wing designs. The high gradients induced by the propeller slip-stream could also result in velocity disturbances which violate small-perturbation assumptions. If this is the case, a full potential equation formulation might be required. In addition, modeling of the slipstream rotational effects could be important and this would suggest a scheme based on Euler's equations. Since computations were eventually to be performed for complex wing-body-nacelle-slipstream arrangements, a study was conducted to identify whether or not there were fundamental limita-tions inherent in the small-perturbation formulation which would compromise even the clean wing flow predictions. If this was indeed the case, the predicted incremental effects caused by the slipstream and the nacelle embedded in the wing would be compromised.

Experimental data provided by Welge & Crowder[8] is useful for evaluating slipstream models. The thick, blunt, supercritical wing shape can also be studied to identify any limitations of the basic small-perturbation approach. Wing-body configuration data for the condition $M = 0.80$, $\alpha = 3°$ are compared to computational predictions in Fig. 2. Full potential code (FLO-22) results[5] are also included. The FLO-22 results do not permit an exact comparison because the body surface and wing viscous effects are not modeled, but an interesting observation can still be made. The high grid density small-perturbation scheme appears to predict details of the wing double shock wave system better than the full potential code.

A similar correlation set was generated for a flow condition of $M = 0.80$, $\alpha = 1.83°$. The computed results[6] obtained with a full potential equation, finite volume formulation (FLO-28) can be superimposed for com-parison purposes. Fig. 3 shows the experiment/analysis agreement for this case, which also exhibits an interesting double shock wave system. The finite volume code predictions do not show good shock wave resolu-tion. This is particularly noticeable at the forward shock location. It is assumed that this resolution problem is related to a smearing effect inherent in the finite volume formulation. The FLO-28 simulation includes the body shape, but apparently no boundary layer was added. This will affect the FLO-28 predicted aft-end load levels, but no significant impact on shock wave resolution is anticipated.

Euler code results[4] were used to construct Fig. 4, which includes comparisons at two wing stations for $M = 0.70$, $\alpha = 3°$ flow and one station for $M = 0.80$, $\alpha = 1.83°$ flow. In this case, the Euler method was coupled with a scheme to predict the wing boundary layer

OOO EXPERIMENT (REF. 8)
XXXXX PRESENT METHOD
——— FLO −22 α = 3.35 (REF. 5)

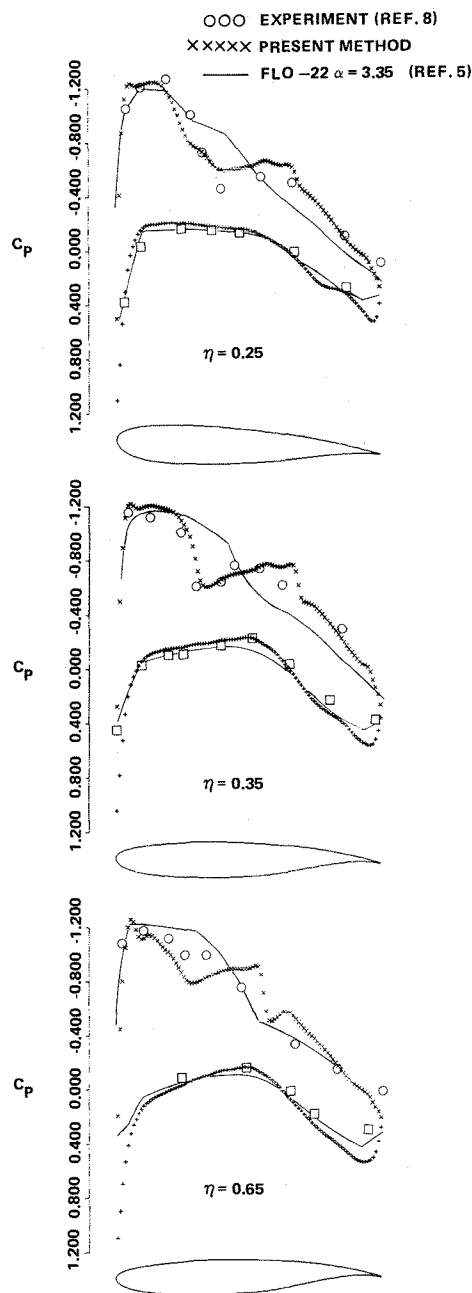η = 0.25

η = 0.35

η = 0.65

R84-0628-002D

Fig. 2 Wing Pressure Distribution Correlation, $M = 0.80$, $\alpha = 3°$

effects. It can be seen that the small-perturbation results show slightly better agreement at the high-speed condi-tion, while the Euler results are slightly better at the low-speed condition.

These analysis/experiment/analysis comparisons indicate that there is no significant penalty associated with the implementation of the small-perturbation scheme for treating wings with blunt, thick, supercritical sections. In fact, the present formulation has demonstrated an ability to resolve flow details better than more sophisti-cated codes. It is conceivable, then, that grid resolution and finite-difference approximations can at times play a more important role in determining flow simulation
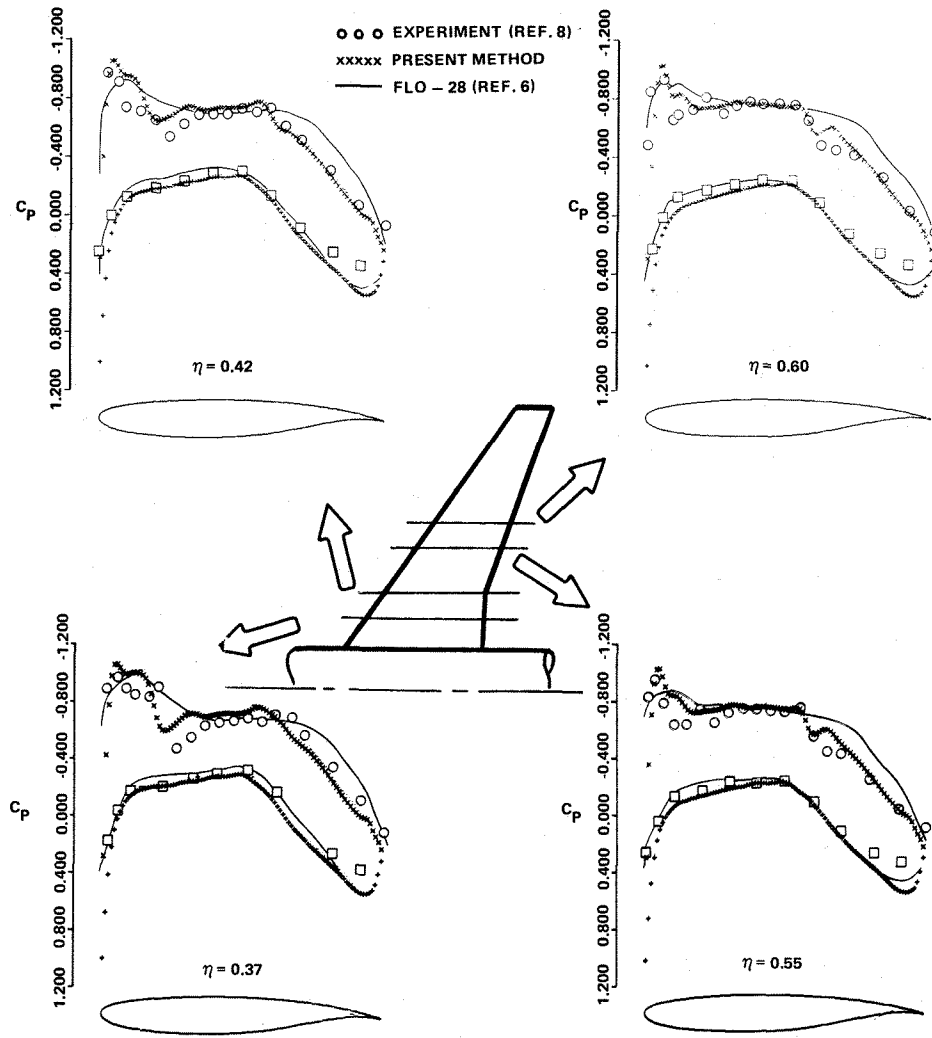
Fig. 3 Wing Pressure Distribution Correlation, M = 0.80, α = 1.83°
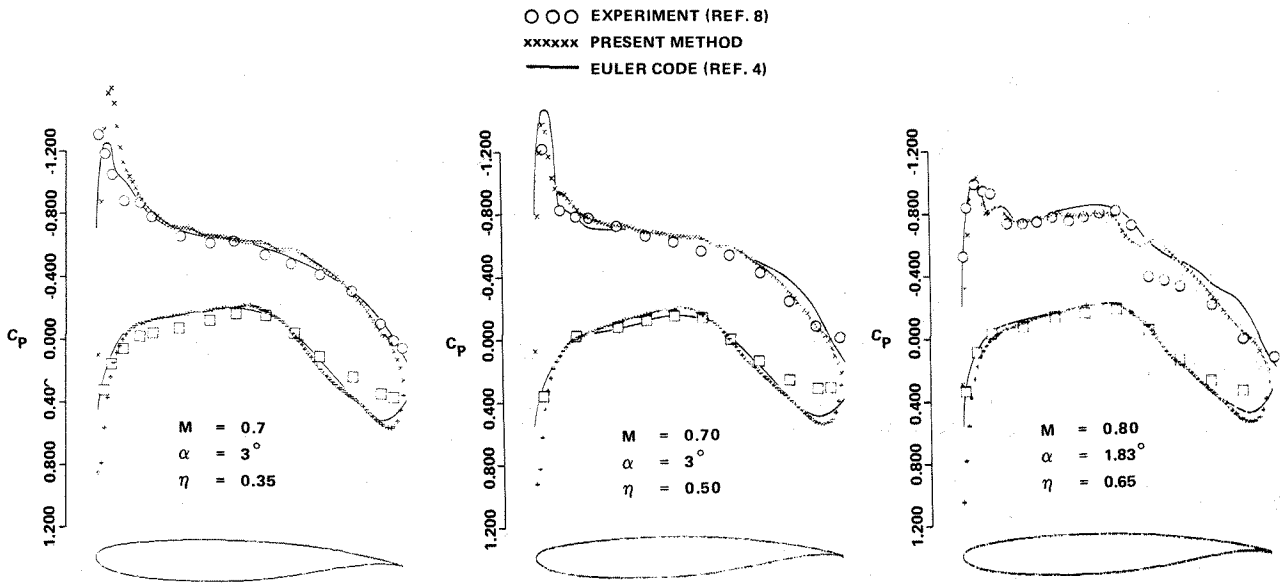
R84-0628-003D

Fig. 4 Wing Pressure Distribution Correlation

R84-0628-004D

583

quality than the terms included in the governing flow equation. With this foundation established, an effort was initiated to predict nacelle and slipstream interference effects.

V. Nacelle Interference Effects

The simulation of an engine nacelle embedded in a wing surface will be a critical component of any computational method applied to the prop-fan installation design problem. Available experimental data[8,9] indicate that the engine pod might have a greater impact on installation drag than the combined effect of the impinging slipstream pressure, velocity, and swirl. The design problem is further compounded because few case studies exist which include a nacelle embedded in a wing at transonic speeds.

The computational method has been modified to permit the modeling of nacelle surfaces which are embedded in wing contours. This has been accomplished by splitting the wing grid relaxation process into two segments. The first represents the region between the fuselage side and the inboard nacelle side. The second region starts at the outboard nacelle side and ends at the wing tip. Special boundary conditions are required to simulate the nacelle side in both regions. Dummy flow field potentials are computed and positioned inside the nacelle; this has been sketched in Fig. 5.
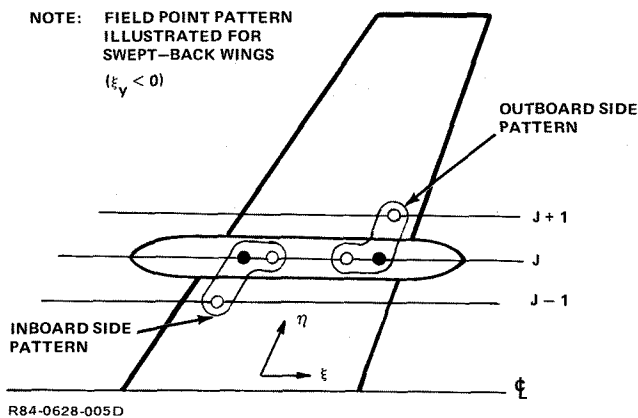

R84-0628-005D

Fig. 5 Grid Points Used to Compute Embedded Nacelle Inboard/ Outboard Boundary Conditions

Special first-order accurate difference operators are employed to ensure a stable relaxation process. The dummy potential values computed for the nacelle outboard side are generated using the following expression:

$$\varphi_{i,j} = \left[\frac{\eta_y}{\Delta\eta}\varphi_{i,j+1} - \frac{\xi_y}{\Delta\xi}\varphi_{i-1,j} - F_x\right] \bigg/ \left(\frac{\eta_y}{\Delta\eta} - \frac{\xi_y}{\Delta\xi}\right) \quad (3)$$

A similar equation is used to compute dummy potential values required to solve for the inboard nacelle side:

$$\varphi_{i,j} = \left[\frac{\eta_y}{\Delta\eta}\varphi_{i,j-1} - \frac{\xi_y}{\Delta\xi}\varphi_{i+1,j} + F_x\right] \bigg/ \left(\frac{\eta_y}{\Delta\eta} - \frac{\xi_y}{\Delta\xi}\right) \quad (4)$$

Both of these expressions are obtained by substituting the appropriate difference approximations (see Fig. 5) in the following equation:

$$\varphi_y = \varphi_\xi\,\xi_y + \varphi_\eta\,\eta_y = F_x \quad (5)$$

This scheme is suitable for simulating the nacelle in the wing embedded fine grid system. Additional provisions must be made for representing the nacelle in the global crude grid system. Numerical experiments suggested that the grid point patterns illustrated in Fig. 6 would be satisfactory. The diamond model is suitable for nacelles which are centrally mounted on the wing. The half-diamond model works well for nacelles which are mounted low.
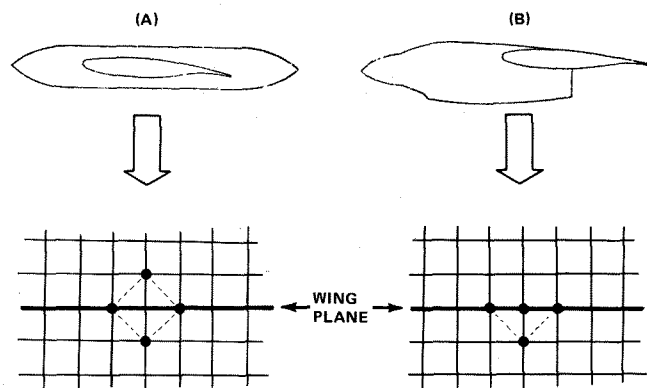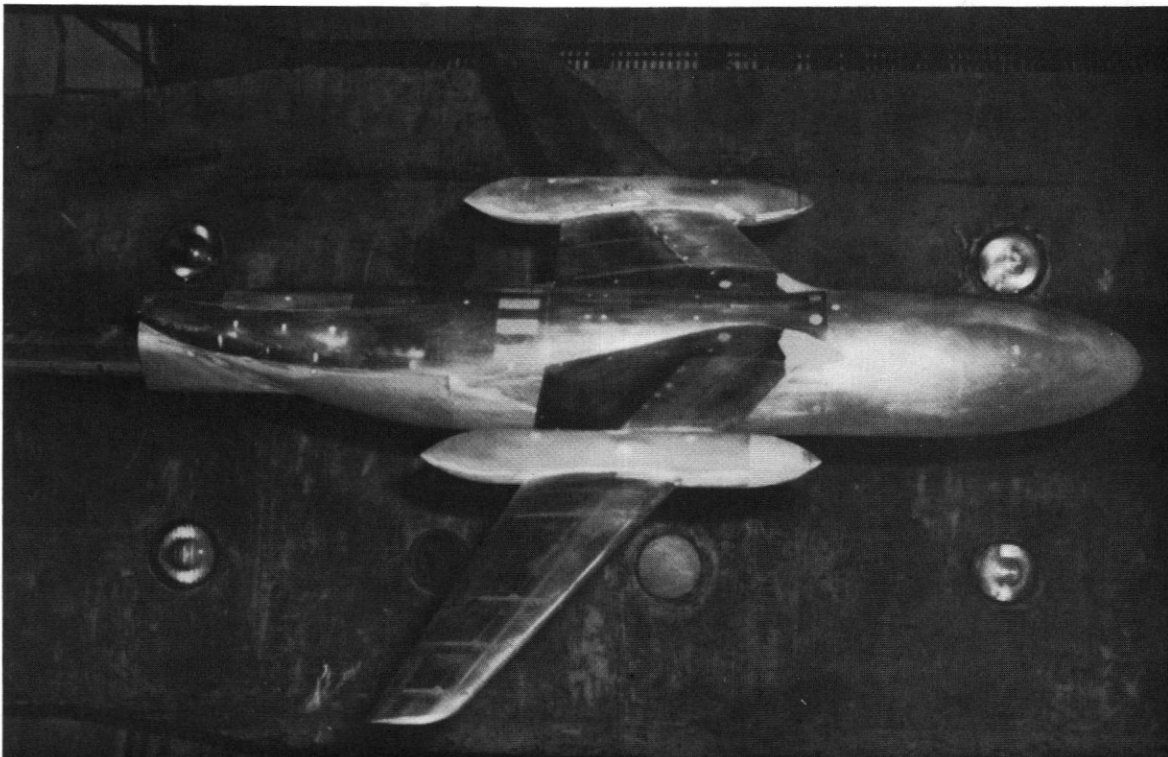

R84-0628-006D

Fig. 6 Nacelle Grid Point Patterns for Central and Low Mount Positions

Turboprop nacelles are typically quite complex, both in contour and orientation on the wing. This presents a modeling problem for validating a new formulation. To rectify this situation, a cooperative effort was initiated with the Propulsion Branch at NASA's Langley Research Center. A test configuration was specifically set up to be as simple as possible for analysis using the computational method. Large nacelle shapes representing a prop-fan pusher or tractor arrangement were mounted at the planform break on a supercritical wing transport configuration designated USB. The pods were centrally mounted above and below the wing, the side contours were straight, and the pod-wing junctures (left and right) were positioned at existing pressure tap rows. This configuration is shown in Fig. 7.

Correlations with experimental data for this special model can be found in Fig. 8. Nacelle on/off effects can be identified. Note that nacelle-off comparisons were performed at M = 0.80, while nacelle-on comparisons were performed at M = 0.75. The lower nacelle-on Mach number was selected because of significant flow separation induced by the nacelle at the higher Mach number. This

R84-0628-007D

Fig. 7 Model of USB Transport With Nacelles Embedded in Wing Surface in NASA LaRC 16ft. Transonic Wind Tunnel
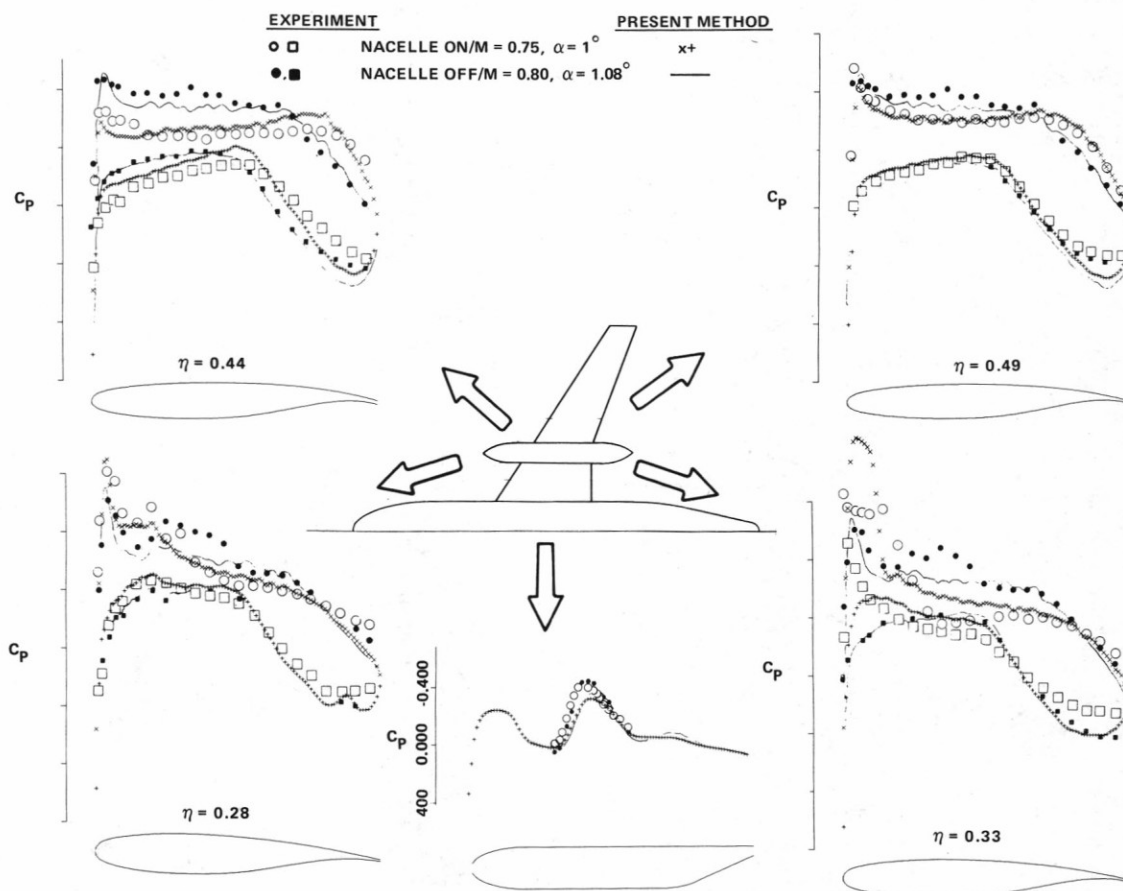
R84-0628-008D

Fig. 8 Effect of Wing-Mounted Nacelle on Wing and Fuselage Pressures for NASA USB Transport

might be attributed to the lack of fairings in the wing-nacelle juncture region. Overall agreement is good but some discrepancies can be identified near the inboard juncture leading edge. This might be attributed to the relatively coarse representation of the nacelle surface in the global crude grid system (32 grid points) and, of course, the possibility of flow separation at the inboard juncture leading edge still exists.

Table 1 provides a comparison of the predicted and experimental lift, drag and moment increments generated by the nacelles. The lack of agreement might be attributable to flow separation at the leading edge of the inboard pod juncture. While a lower Mach number (M = 0.75) was chosen to minimize this effect, it can be seen that the pressure distribution predicted by the computational method indicates that the Mach number before the shock wave is greater than 1.5. This suggests that the flow might be separated despite the fact that the boundary layer scheme predicts no separation.

TABLE 1 EFFECT OF NACELLES ON FORCE AND MOMENT COEFFICIENTS

	EXPMT	PRESENT METHOD
Δc_L	- 0.0560	- 0.0310
Δc_M	+0.0200	+0.0120
Δc_D	- 0.0004	- 0.0021
R84-0628-009D		

A second comparison set was generated using the wing-body-nacelle data of Smith & Levin[9]. Correlations with experimental data can be found in Fig. 9. Recall that the nacelle-off results for this condition were presented in Fig. 3. The dramatic interference effect induced by the nacelle is satisfactorily reproduced except for the expansions apparent on the wing lower surface. This discrepancy might be caused by the codes inability to simulate the high pressure region aft of the nacelle

OOO EXPERIMENT (REF. 9)
XXXX PRESENT METHOD

$\eta = 0.42$

$\eta = 0.60$

$\eta = 0.37$

$\eta = 0.55$
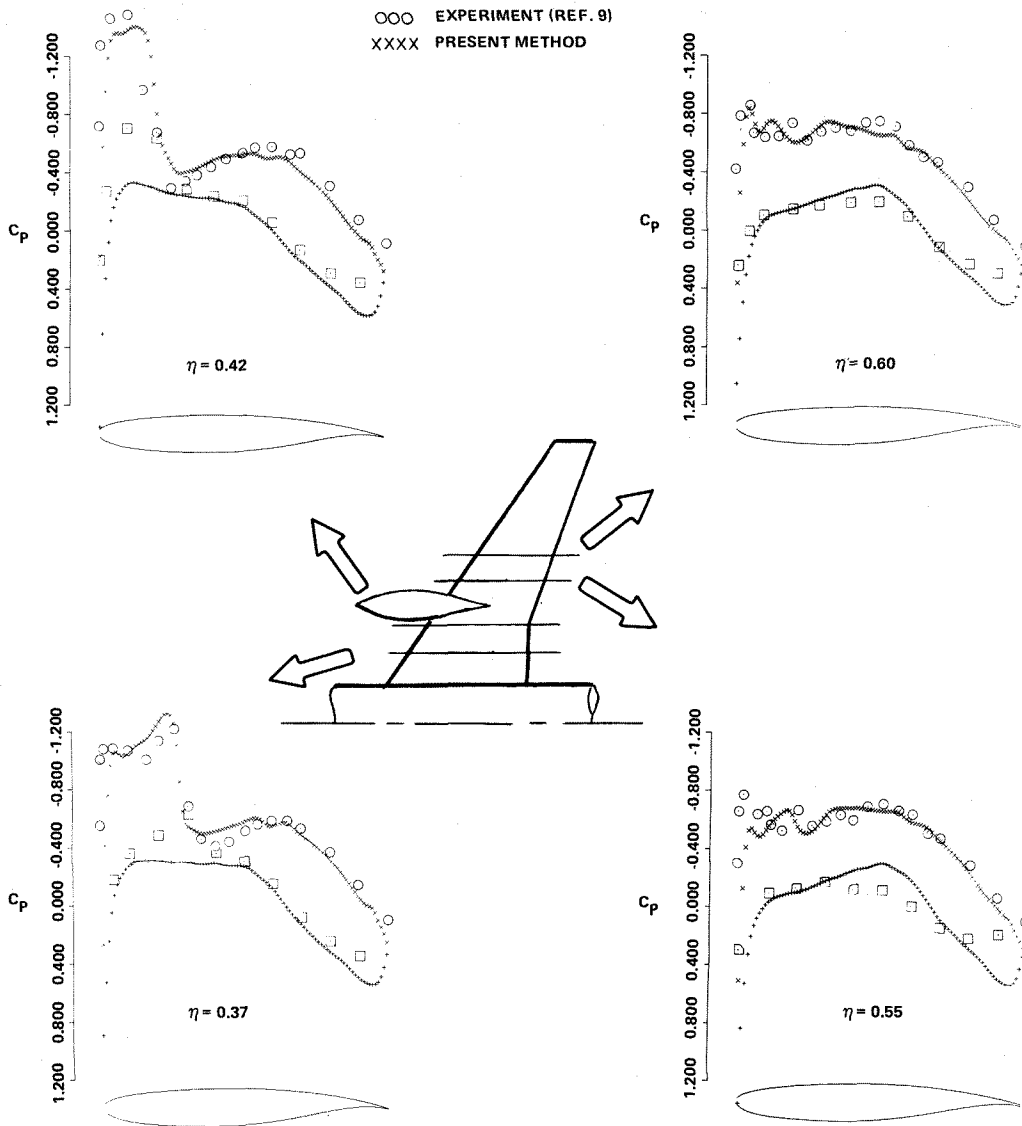
R84-0628-010D

Fig. 9 Wing-Body-Nacelle Pressure Distribution Correlation, M = 0.80, α = 1.83°

base (recall Fig. 6B) which abruptly ends. Unlike the USB case, however, no flow separation is apparent.

VI. Slipstream Modeling

The prop-fan slipstream is a region of high energy, rotational flow. The additional energy, which can be quantified in terms of the increase in total pressure and temperature, will translate into increased Mach number and dynamic pressure as the flow leaves the blade plane. A swirl is also imparted to the flow as it passes the prop-fan blades. The distributions of these properties will change as the flow proceeds downstream about the airframe components and viscous effects will eventually dissipate the slipstream flow. Modeling all of these characteristics would be quite difficult and, therefore, the need exists to determine how simple the slipstream model can be and still provide useful engineering design information.

The basic algorithm described in Section II was modified to incorporate a slipstream simulation. Modeling the flow within the slipstream as a small perturbation to the undisturbed slipstream's ultimate wake, equation (1) is employed using

$$M_\infty = M_\infty (r) = \sqrt{5(1 + 0.2 \, M_\infty^2) \left(\frac{P_T(r)}{P_{T_\infty}}\right)^{\frac{\gamma-1}{\gamma}} - 1} \quad (6)$$

Here $P_T(r)/P_{T_\infty}$ represents the ratio of total pressure in the slipstream to that in the freestream, and $M_\infty(r)$ is the Mach number in the slipstream ultimate wake (assuming isentropic flow so $P = P_\infty$). The pressure coefficient given by equation (2) is then corrected to freestream dynamic pressure

$$C_P = \frac{P - P_\infty}{q_\infty} = \frac{P - P_\infty}{q_\infty(r)} \frac{q_\infty(r)}{q_\infty}$$

$$= - \left[2\varphi_x + (1 - M_\infty^2(r)) \, \varphi_x^2 + \varphi_y^2\right] \frac{M_\infty^2(r)}{M_\infty^2} \quad (7)$$

Finally, slipstream swirl velocities are superimposed on the otherwise irrotational flow. This requires a modification to the standard planar wing boundary condition

$$\varphi_z = \frac{dz}{dx} - \alpha \quad (8)$$

to give

$$\varphi_z = \frac{dz}{dx} - \alpha - W(r) \quad (9)$$

where $W(r)$ represents the slipstream swirl.

The radial Mach distribution, given by equation (6), is enforced by adjusting the Mach number for each spanwise plane along the wing which lies within the slipstream region. This represents a very coarse approximation since the physical flow Mach variations are constrained to the cylindrical slipstream volume while the computational Mach variation extends to vertical infinity above and below the wing using the present Cartesian scheme. While a cylindrical grid system would obviate the need for this approximation, correlations with experimental data indi-

cate that there is no significant penalty associated with its use.

Total pressure and swirl data[8] for a slipstream simulator appear in Fig. 10. The computational distributions indicated in the figure were obtained by treating spanwise grid stations as cell centerlines and then using the average value across each cell width. This procedure proved quite valid though some smearing of slipstream properties probably occurs. Figure 11 compares computed and experimental wing pressure distributions using this simple slipstream model at $M = 0.80$ for $\pm 7°$ swirl. Recall that the basic or clean wing pressure comparisons for this condition were included in Fig. 2. The effect of the two slipstreams on the wing spanwise loading can be found in Fig. 12. The incremental lift and drag levels can be found in Fig. 13. It can be seen that detailed pressure distributions agree quite well but, surprisingly, the drag and lift increments agree better with the incompressible theory than with the experimental data.

A similar set of comparisons was prepared using propeller-generated slipstream data[9]. These correlations are compromised somewhat by a separated flow region inboard of the nacelle (see Fig. 14). Unlike the USB-nacelle case (Fig. 8), however, the boundary layer method did predict that flow separation would occur at the two inboard wing stations. Note that comparisons without the slipstream were included in Fig. 9.
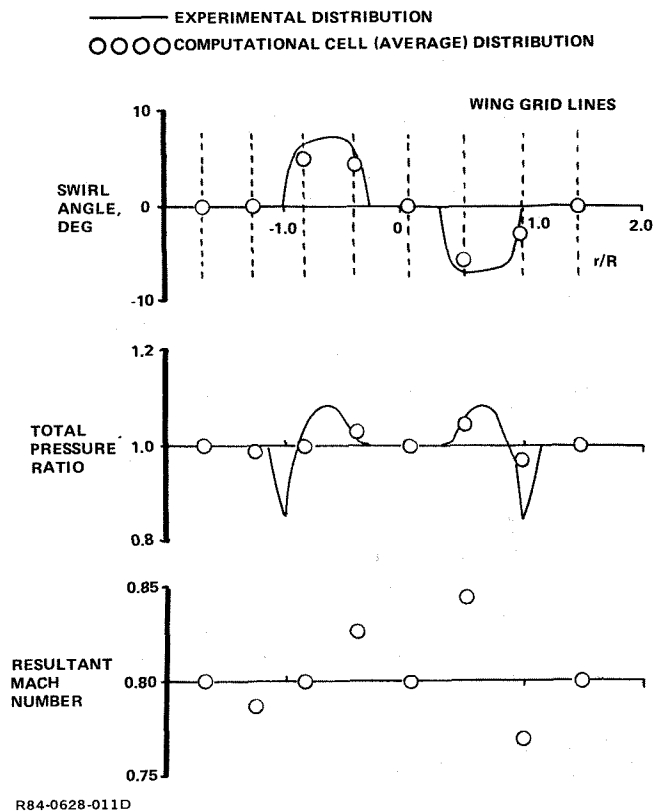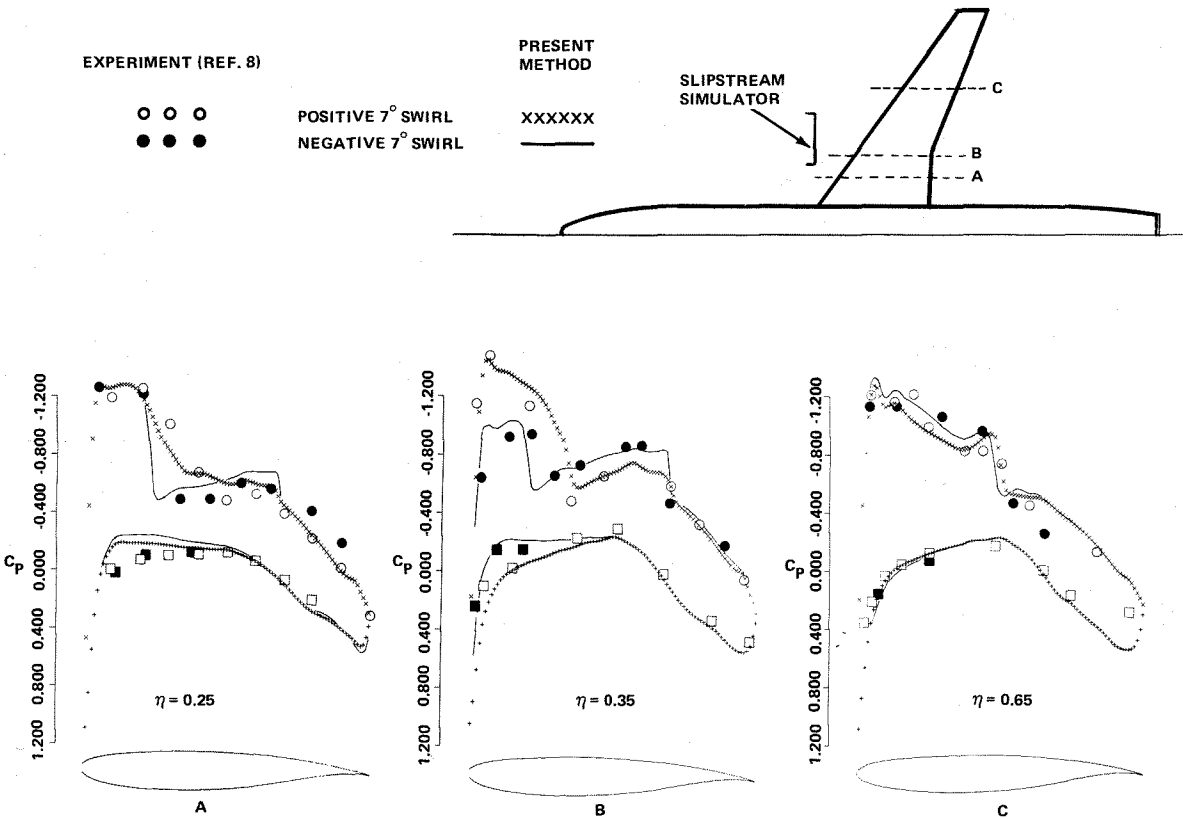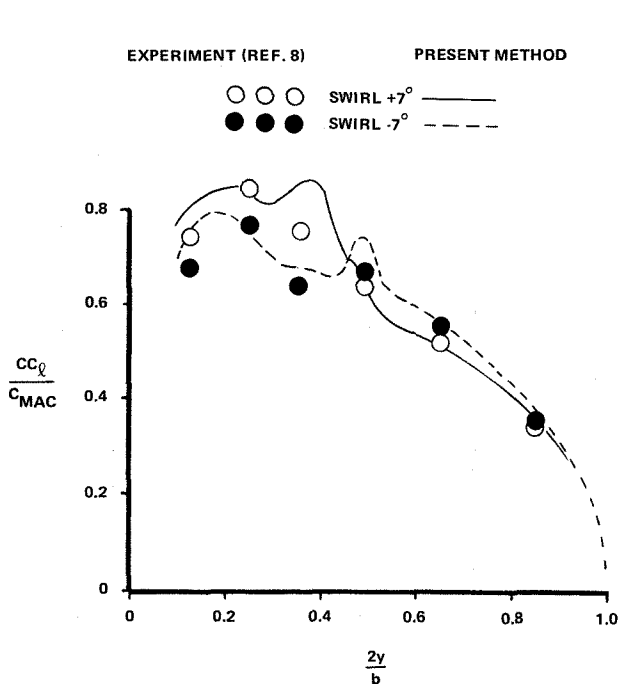

R84-0628-011D

Fig. 10 Experimental/Computational Swirl, Total Pressure, and Mach Number Distributions

EXPERIMENT (REF. 8)

PRESENT METHOD

POSITIVE 7° SWIRL   XXXXXX
NEGATIVE 7° SWIRL   ———

SLIPSTREAM SIMULATOR

$\eta = 0.25$ $\eta = 0.35$ $\eta = 0.65$

A   B   C
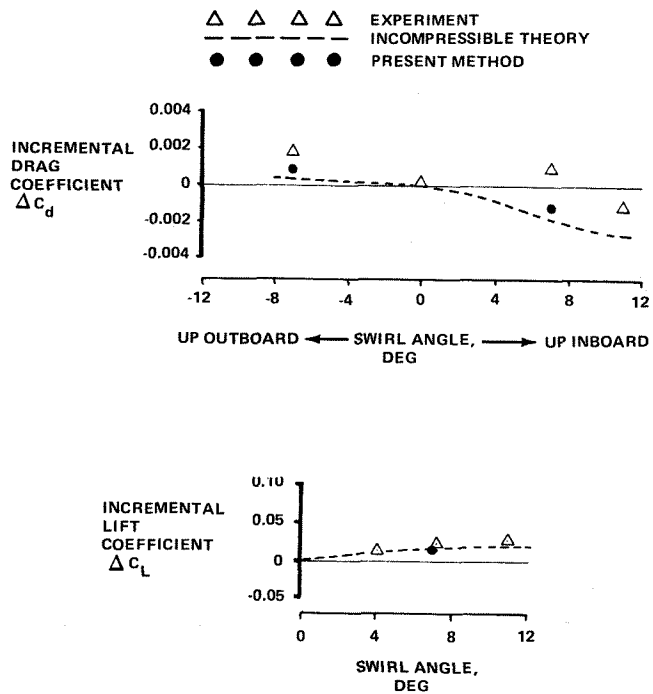
R84-0628-012D

Fig. 11 Wing Pressure Distribution Correlations for Positive and Negative Swirl, M = 0.80, $\alpha = 3°$

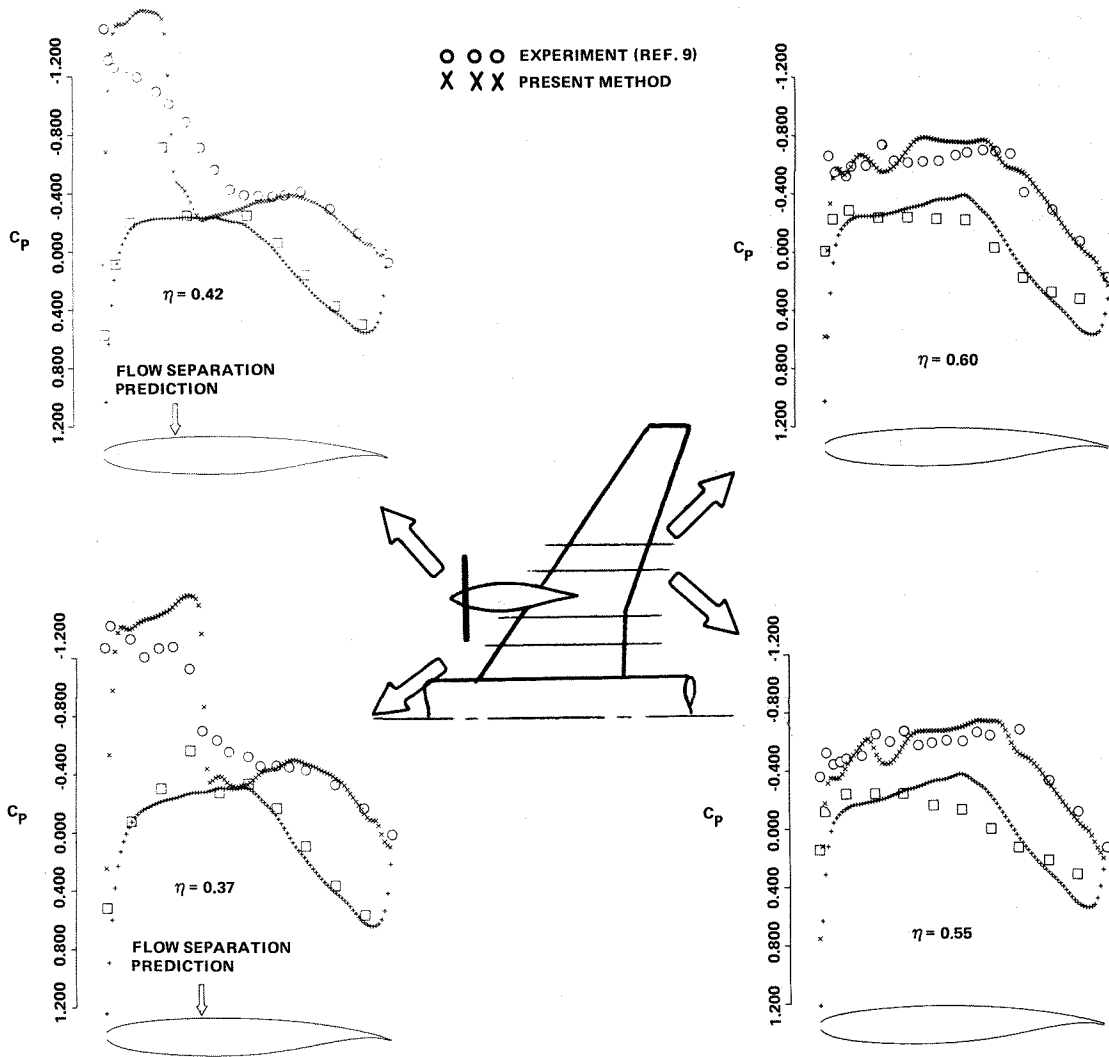EXPERIMENT (REF. 8)   PRESENT METHOD

SWIRL +7° ———
SWIRL -7° — — —

$\frac{cc_\ell}{c_{MAC}}$

$\frac{2y}{b}$

R84-0628-013D

Fig. 12 Effect on Swirl on Wing Spanload, M = 0.80

EXPERIMENT
INCOMPRESSIBLE THEORY
PRESENT METHOD

INCREMENTAL DRAG COEFFICIENT Δc_d

UP OUTBOARD ◄— SWIRL ANGLE, DEG —► UP INBOARD

INCREMENTAL LIFT COEFFICIENT Δc_L

SWIRL ANGLE, DEG

R84-0628-014D

Fig. 13 Effect of Slipstream Swirl on Configuration Lift and Drag, M = 0.80

O O O EXPERIMENT (REF. 9)
X X X PRESENT METHOD

R84-0628-015D

Fig. 14 Wing-Body-Nacelle Slipstream Pressure Distribution Correlation, M = 0.80, $\alpha = 1.83°$

VII. Concluding Remarks

1. A transonic small-perturbation scheme appears to be quite satisfactory for prop-fan engine installation analyses. Current flow modeling capability is more constrained by the ability to satisfactorily predict and simulate separated flow regions (Fig. 8, 14) than it is by the ability to simulate large disturbances induced by nacelles, slipstreams, and blunt supercritical airfoil sections (Fig. 9, 11). While the physical flow features unsteadiness and vorticity, it is not clear at this point in time what benefits will be obtained by explicitly modeling these aspects of the flow field.

2. Computational grid density and differencing scheme approximations appreciably affect shock wave resolution. For some applications, these factors will play a more important role in determining flow simulation quality than the terms which are included in the flow governing equation.

3. A large portion of the experimental data now used to validate computational schemes for prop-fan nacelle and slipstream models features separated flow. Comparisons which use these data require careful interpretation.

4. Flow separation has compromised an attempt to evaluate incremental force and moment prediction capability for both a simple nacelle (Table 1) and a propeller-generated slipstream (Fig. 14). For what appears to be attached flow, drag increments obtained using a slipstream simulator (Fig. 13) may be affected by simulator hardware upstream of the model.

VIII. References

1. Boctor, M.L., Clay, C.W., and Watson, C.F., "An Analysis of Prop-fan/Airframe Aerodynamic Integration," NASA CR-152186, Oct 1978.

589

2. Rizk, M.H., "Aerodynamic Effects of Nearly Uniform Slipstreams on Thin Wings in the Transonic Regime," NASA CR-152351, May 1980.

3. Welge, H.R., Neuhart, D.H., and Dahlin, J.A., "Analysis of Mach Number 0.8 Turboprop Slipstream Wing/Nacelle Interactions," NASA CR-166214, Aug 1981.

4. Whitfield, D.L. and Jameson, A., "Three-Dimensional Euler Equation Simulation of Propeller-Wing Interaction in Transonic Flow,," AIAA Paper 83-0236, Jan 1983.

5. Narain, J.P., "A Transonic Analysis of Propfan Slipstream Effect on a Supercritical Wing," AIAA Paper 83-0186, Jan 1983.

6. Samant, S.S., Yu, N.J., and Rubbert, P.E., "Transonic Flow Simulation of Propfan Configurations," AIAA 83-0187, Jan 1983.

7. Boppe, C.W., "Transonic Flow Field Analysis for Wing-Fuselage Configurations," NASA CR-3243, May 1980.

8. Welge, H.R. and Crowder, J.P., "Simulated Propeller Slipstream Effects on a Supercritical Wing," NASA CR-152138, June 1978.

9. Smith, R.C. and Levin, A.D., "Propfan Installation Aerodynamics of a Supercritical Swept Wing Transport Configuration," AIAA 81-1563, July 1981.

10. Bradshaw, P. and Ferriss, D.H., "Calculation of Boundary Layer Development Using the Turbulent Energy Equations. Compressible Flow on Adiabatic Walls," J. Fluid Mech, Vol 46, 1971.

11. Nash, J.F. and Tseng, R.R., "The Three-Dimensional Turbulent Boundary Layer On an Infinite Yawed Wing," The Aeronautical Quarterly, November 1971, pp 346-262.